

## JWST Imaging of the Cartwheel Galaxy Reveals Dust Formation in SN 2021afdx

GRIFFIN HOSSEINZADEH <sup>1</sup>, DAVID J. SAND <sup>1</sup>, JACOB E. JENCON <sup>2</sup>, JENNIFER E. ANDREWS <sup>3</sup>, IRENE SHIVAEI <sup>1</sup>,  
K. AZALEE BOSTROEM <sup>1,\*</sup>, STEFANO VALENTI <sup>4</sup>, TAMÁS SZALAI <sup>5,6,7</sup>, JAMISON BURKE <sup>8,9</sup>,  
D. ANDREW HOWELL <sup>8,9</sup>, CURTIS MCCULLY <sup>8,9</sup>, MEGAN NEWSOME <sup>8,9</sup>, ESTEFANIA PADILLA GONZALEZ <sup>8,9</sup>,  
CRAIG PELLEGRINO <sup>8,9</sup> AND GIACOMO TERRERAN <sup>8,9</sup>

<sup>1</sup>*Steward Observatory, University of Arizona, 933 North Cherry Avenue, Tucson, AZ 85721-0065, USA*

<sup>2</sup>*Department of Physics and Astronomy, The Johns Hopkins University, 3400 North Charles Street, Baltimore, MD 21218, USA*

<sup>3</sup>*Gemini Observatory, 670 North A‘ohoku Place, Hilo, HI 96720-2700, USA*

<sup>4</sup>*Department of Physics and Astronomy, University of California, Davis, 1 Shields Avenue, Davis, CA 95616-5270, USA*

<sup>5</sup>*Department of Experimental Physics, Institute of Physics, University of Szeged, Dóm tér 9, Szeged, 6720 Hungary*

<sup>6</sup>*ELKH-SZTE Stellar Astrophysics Research Group, H-6500 Baja, Szegedi út, Kt. 766, Hungary*

<sup>7</sup>*Konkoly Observatory, Research Centre for Astronomy and Earth Sciences, Eötvös Loránd Research Network (ELKH), Konkoly-Thege Miklós út 15-17, 1121 Budapest, Hungary*

<sup>8</sup>*Las Cumbres Observatory, 6740 Cortona Drive, Suite 102, Goleta, CA 93117-5575, USA*

<sup>9</sup>*Department of Physics, University of California, Santa Barbara, CA 93106-9530, USA*

(Received 2022 October 12)

Submitted to The Astrophysical Journal Letters

### ABSTRACT

We present near- and mid-infrared (0.9–18  $\mu\text{m}$ ) photometry of supernova (SN) 2021afdx, which was imaged serendipitously with the James Webb Space Telescope (JWST) as part of its Early Release Observations of the Cartwheel Galaxy. Our ground-based optical observations show it is likely to be a Type IIb SN, the explosion of a yellow supergiant, and its infrared spectral energy distribution (SED)  $\approx 200$  days after explosion shows two distinct components, which we attribute to hot gas and warm dust in the SN ejecta. By fitting models of dust emission to the SED, we derive a lower limit on the dust mass of  $>2.8 \times 10^{-3} M_{\odot}$ , which is the highest yet observed in a Type IIb SN but consistent with other Type II SNe observed by the Spitzer Space Telescope. We also find that the radius of the dust is consistent with the radius of the ejecta, as derived from spectroscopic velocities during the photospheric phase, which could imply that the dust formed inside the ejecta. However, we cannot rule out an infrared echo off of pre-existing dust in the progenitor environment. Our results show the power of JWST to address questions of dust formation in SNe, and therefore the presence of dust in the early Universe, with much larger samples than have been previously possible.

*Keywords:* Core-collapse supernovae (304), Supernovae (1668), Type II supernovae (1731), Dust formation (2269)

### 1. INTRODUCTION

Radio observations of luminous quasars in the early Universe (redshift  $z \gtrsim 6$ , age  $\lesssim 1$  Gyr) show them to be large dust reservoirs ( $\gtrsim 10^8 M_{\odot}$ ; Bertoldi et al. 2003; Gall et al. 2011a; Hashimoto et al. 2019; though see

Bakx et al. 2020 for a recent counterexample). With progenitor lifetimes of only tens of Myr, dust condensation in the expanding ejecta of core-collapse supernovae (SNe) has been proposed as the major source of dust in these early galaxies (see Gall et al. 2011b for a review). Models developed for this purpose require rapid dust production of up to  $1 M_{\odot}$  per SN during the first 1–2 years after explosion (e.g., Dwek et al. 2007, 2019, but see Wesson & Bevan 2021 for an alternate discus-

Corresponding author: Griffin Hosseinzadeh  
griffin0@arizona.edu

\* LSSTC Catalyst Fellow

sion). However, nebular observations of SNe in the local Universe have for the most part not directly confirmed these large dust masses. Compilations of near- and mid-infrared (IR) observations of SNe yield warm dust masses in the range of  $10^{-6}$  to  $10^{-2} M_{\odot}$  (Szalai & Vinkó 2013; Tinyanont et al. 2016; Szalai et al. 2019).

When the search for SN dust extends to even older SNe, or into the far-IR or radio wavelengths, there is less of a discrepancy between the required and observed dust masses. For example, unambiguous evidence of  $0.4\text{--}0.7 M_{\odot}$  of newly formed cold dust has been confirmed with Herschel and ALMA observations of SN 1987A (Matsuura et al. 2011; Indebetouw et al. 2014). Additionally, large masses of cold dust have been detected in much older Galactic SN remnants (Barlow et al. 2010; Gomez et al. 2012; Arendt et al. 2014; Lau et al. 2015; Temim et al. 2017), suggesting significant amounts of dust formation occurring in the decades after explosion.

Thermal dust emission typically peaks in the mid-IR ( $5\text{--}10 \mu\text{m}$ ), putting it out of reach of ground-based observations. Until now, the state of the art in observations of dust in extragalactic SNe was using the Spitzer Space Telescope before it ran out of cryogen in 2009 (the Spitzer Cold Mission) to observe the full near-IR to mid-IR spectral energy distribution (SED) of 12 SNe II (Kotak et al. 2005, 2006, 2009; Meikle et al. 2007; Andrews et al. 2011; Meikle et al. 2011; Szalai et al. 2011; see Szalai & Vinkó 2013 and Priestley et al. 2020 for the full sample). Since then, Spitzer has observed dozens more SNe out to  $4.5 \mu\text{m}$  during its Warm Mission (Tinyanont et al. 2016; Szalai et al. 2019), but in this wavelength regime, the thermal and line emission from the SN ejecta can dominate over any dust emission, so it is difficult to measure dust properties and masses.

An additional complication is the fact that dust masses cannot be fully constrained when the dust is optically thick (e.g., Meikle et al. 2007). A large amount of dust can be hidden behind an optically thick surface layer without changing the observed SED. This happens at dust masses around  $10^{-3} M_{\odot}$  (Meikle et al. 2007), although this number also depends on the dust radius and composition. Therefore it is possible that many of the previous dust measurements are in fact lower limits.

The first images from the James Webb Space Telescope (JWST) were released on 2022 July 12 (Pontoppidan et al. 2022), reopening our window into the space-based mid-IR. Images of the Cartwheel Galaxy, taken with the Near-Infrared Camera (NIRCam; Rieke et al. 2005) and the Mid-Infrared Instrument (MIRI; Rieke et al. 2015), were released shortly thereafter, on 2022 August 2 (Figure 1). As first noted by Engesser et al.

(2022), SN 2021afdx is detected in these images, taken at phases of 197 (NIRCam) and 200 (MIRI) rest-frame days after the last predisccovery nondetection.

In this Letter, we use these images to construct the full near- to mid-IR SED of SN 2021afdx with the goal of constraining dust formation in its ejecta, the first opportunity to do this type of analysis in the past decade. In Section 2.1, we describe our supporting ground-based optical observations, and in Section 2.2, we measure photometry on the space-based IR images. We fit dust models to the resulting SED and compare to previous measurements in Section 3. In Section 4, we investigate whether the dust was newly formed in the SN ejecta or whether it existed in the progenitor environment before explosion. We conclude by looking forward to the future of SN dust measurements with JWST in Section 5.

## 2. OBSERVATIONS AND DATA REDUCTION

### 2.1. Ground-based Optical

SN 2021afdx was discovered by the Asteroid Terrestrial-impact Last Alert System (ATLAS; Tonry et al. 2018) on 2021 November 23.308 UT at right ascension  $00^{\text{h}}37^{\text{m}}42^{\text{s}}.580$  and declination  $-33^{\circ}43'25''.28$  (Tonry et al. 2021),  $32''$  southeast of the center of the Cartwheel Galaxy (ESO 350-40). We downloaded the full survey light curve from the ATLAS Forced Photometry Server. The explosion time is not very well constrained, as the transient only peaked  $\approx 1.5$  mag above the typical limiting magnitude of the survey, so we adopt the last predisccovery nondetection on 2021 November 21.352 UT as phase = 0 throughout our analysis.

We also obtained multiband follow-up photometry using the Sinistro cameras on Las Cumbres Observatory’s network of 1 m telescopes (Brown et al. 2013) as part of the Global Supernova Project. We subtracted reference images of the field taken with the same telescopes on 2022 May 27, about 4 months after the SN had faded, using PyZOGY (Guevel & Hosseinzadeh 2017) and measured PSF photometry on the difference images using `lcogtspipe` (Valenti et al. 2016). We calibrated this photometry to the AAVSO Photometry All-Sky Survey (Henden et al. 2009).  $B$  and  $V$  are reported in Vega magnitudes, and  $g$ ,  $r$ , and  $i$  are reported in AB magnitudes.

We adopt a luminosity distance of  $d_L = 136.8$  Mpc (distance modulus  $\mu = 35.68$  mag) based on the redshift of the Cartwheel Galaxy ( $z = 0.030187$ ; Amram et al. 1998) and the cosmology of the Planck Collaboration (2020). Absolute magnitudes are corrected for Milky Way extinction of  $E(B - V) = 0.0092$  mag (Schlafly & Finkbeiner 2011) using the Fitzpatrick (1999) extinction

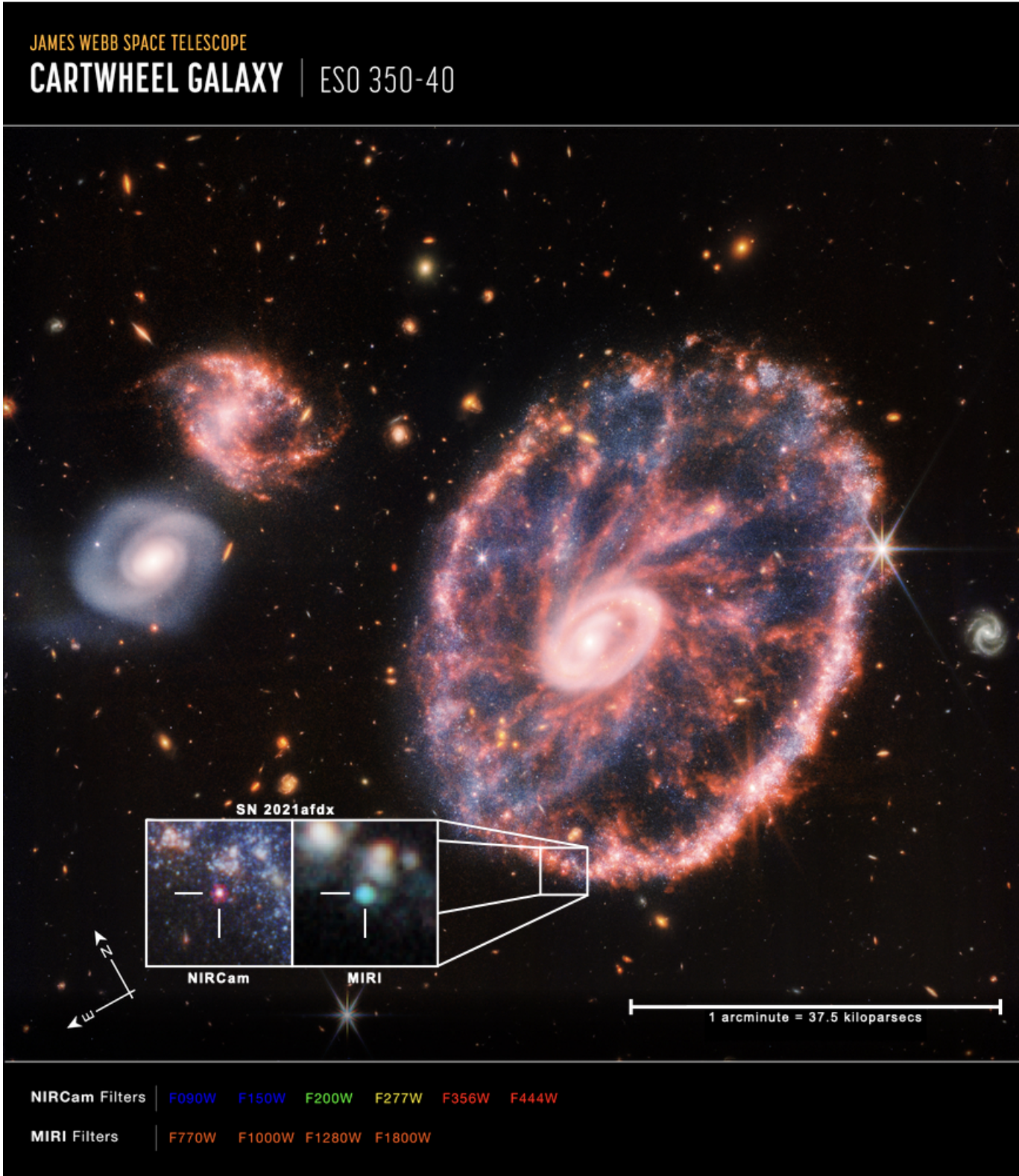


**Figure 1.** Composite image of the Cartwheel Galaxy taken with JWST’s NIRCam and MIRI instruments, with 7.6'' × 7.6'' insets of SN 2021afdx. Credit: NASA, ESA, CSA, STScI, Webb ERO Production Team.

**Table 1.** Spectroscopic Observations and Velocities

| MJD       | Telescope | Instrument | Phase (d) | H $\alpha$ Velocity (Mm s $^{-1}$ ) |
|-----------|-----------|------------|-----------|-------------------------------------|
| 59550.492 | FTS       | FLOYDS     | 10.8      | 12.59 $\pm$ 0.07                    |
| 59557.503 | FTS       | FLOYDS     | 17.6      | 11.70 $\pm$ 0.07                    |
| 59561.491 | FTS       | FLOYDS     | 21.5      | 12.1 $\pm$ 0.1                      |
| 59572.494 | FTS       | FLOYDS     | 32.2      | 11.9 $\pm$ 0.1                      |
| 59583.469 | FTS       | FLOYDS     | 42.8      | 11.1 $\pm$ 0.1                      |
| 59601.425 | FTS       | FLOYDS     | 60.3      | ...                                 |

law. Figure 2 (top) shows the ground-based optical light curve.

We construct a pseudobolometric light curve by fitting a blackbody SED to each epoch of photometry to get the photospheric temperature and radius, using a Markov-chain Monte Carlo (MCMC) routine implemented in the Light Curve Fitting package (Hosseinzadeh & Gomez 2020). We then integrate this SED from the  $U$  to  $I$  bands to obtain a pseudobolometric luminosity that is comparable to previous optical-only data sets. The results are shown in Figure 2 (center and bottom). The peak occurs at a phase of 11.8 d, with a pseudobolometric luminosity of  $L_{\text{peak}} = 1.66 \times 10^{42}$  erg s $^{-1}$  and a photospheric temperature of  $T_{\text{peak}} = 6900$  K.

SN 2021afdx was classified as a SN II by the Advanced Extended Public ESO Spectroscopic Survey of Transient Objects (ePESSTO+; Smartt et al. 2015) based on a spectrum taken with the ESO Faint Object Spectrograph and Camera 2 (EFOSC2; Buzzoni et al. 1984) on the New Technology Telescope on 2021 November 26.173 (Ragosta et al. 2021a). We obtained six additional optical spectra using FLOYDS on Las Cumbres Observatory’s 2 m Faulkes Telescope South (Brown et al. 2013), which are logged in Table 1 and plotted in Figure 3.

Type IIb SNe are a transitional class of core-collapse explosions in which early spectra show strong hydrogen lines that fade away in later spectra (see Gal-Yam 2016 for a review). These are thought to come from partially stripped yellow supergiant progenitors (see reviews by Smartt 2009 and Van Dyk 2016). Ragosta et al. (2021b) raised the possibility of a Type IIb subclassification for SN 2021afdx in their initial AstroNote, based on spectroscopic similarities to SN 2008aq. Several aspects of our data support this classification. First, the absorption component of the H $\alpha$  P Cygni profile is very strong, broad, and asymmetrical compared to typical SN II, and more closely resembles Type IIb spectra. We show this

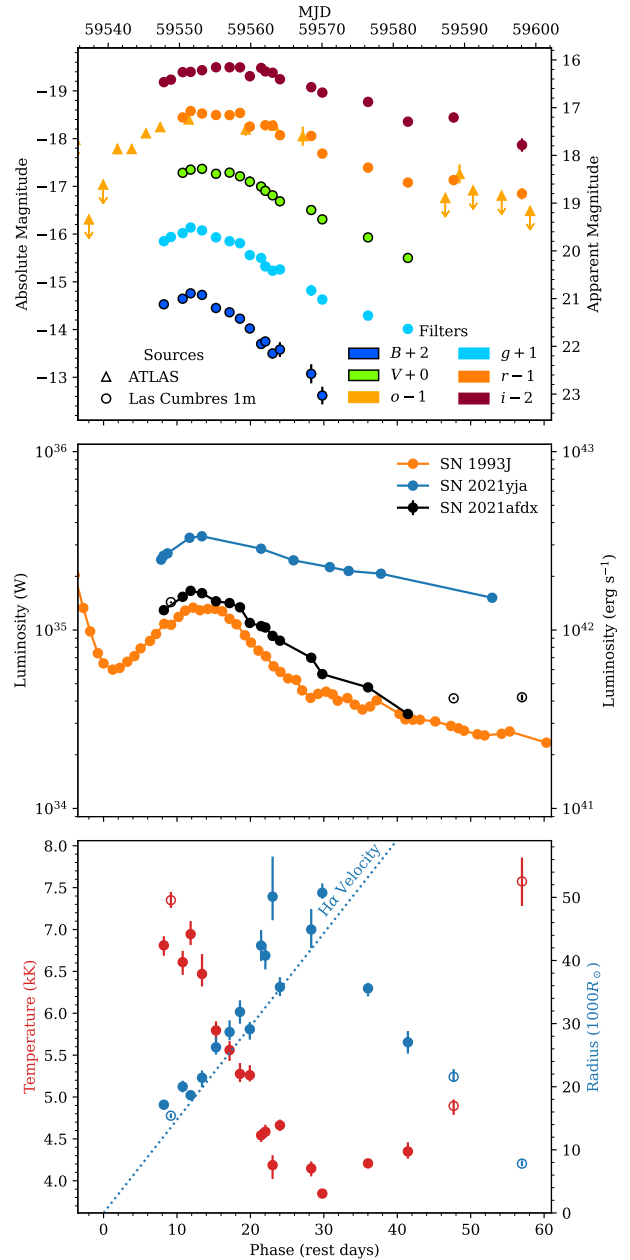


**Figure 2.** Top: Ground-based optical light curve of SN 2021afdx from ATLAS and Las Cumbres Observatory, corrected for Milky Way extinction. Arrows indicate  $3\sigma$  nondetections. Phases are given with respect to the last pre-discovery nondetection. Center: Pseudobolometric ( $U$  to  $I$ ) light curve of SN 2021afdx compared to the pseudobolometric light curves of the Type IIb SN 1993J and the Type II SN 2021yja, approximately aligned to their peak phase. Open markers indicate epochs with detections in only 2 filters, which may not yield reliable luminosity or temperature measurements. The gradual rise and decline of SN 2021afdx, rather than a rapid rise to a plateau, suggests a Type IIb classification. Bottom: The photospheric temperature (red; left axis) and radius (blue; right axis) of SN 2021afdx derived from the data above. The dotted line shows that the ejecta radius inferred from the measured H $\alpha$  velocity is consistent with the photospheric radius around peak. (The data used to create this figure are available.)

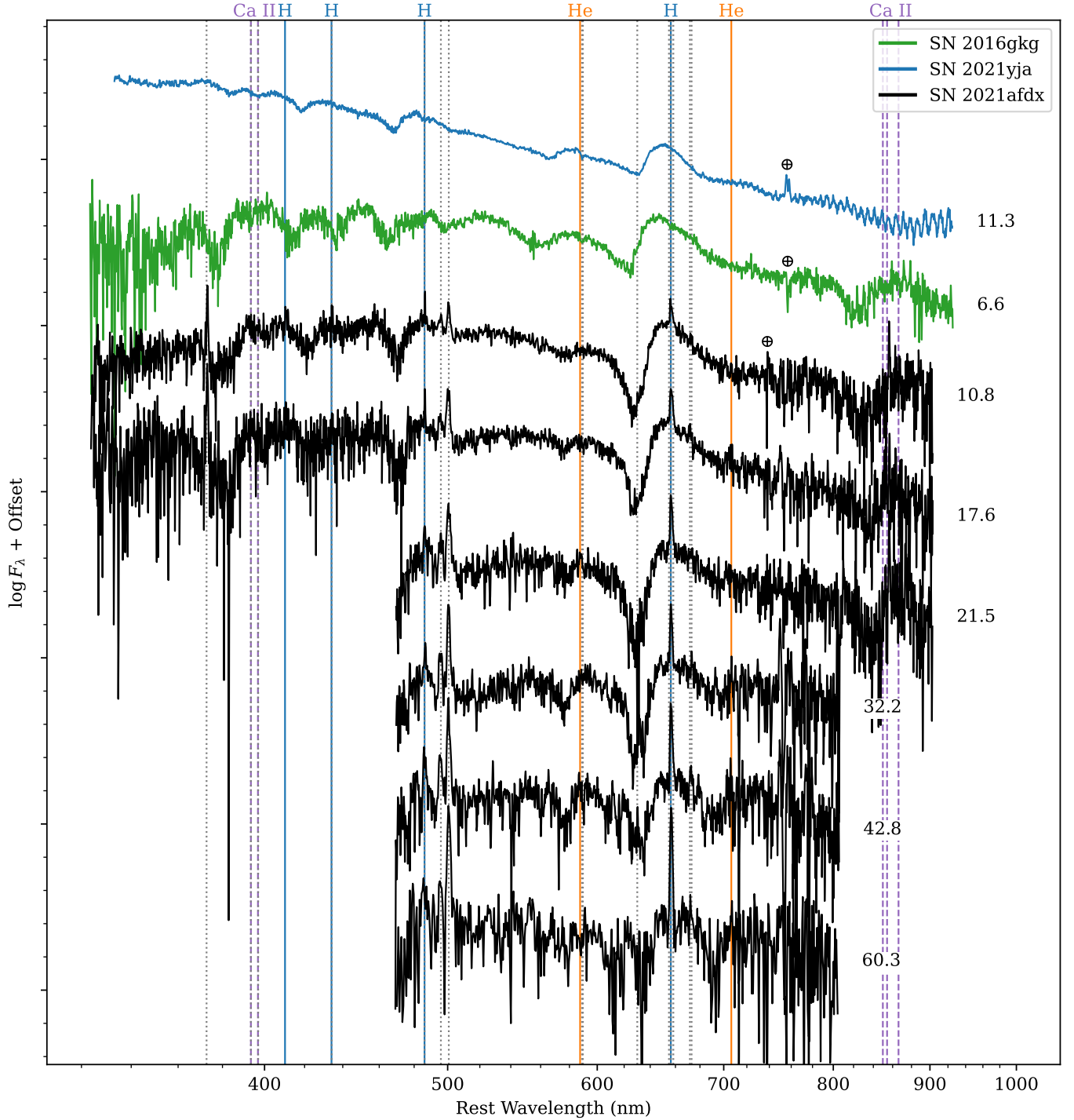


**Figure 3.** Spectral series of SN 2021afdx compared to spectra of the Type IIb SN 2016gkg and the Type II SN 2021yja, all from FLOYDS. Phases are given to the right of each spectrum in rest-frame days. The latest spectrum is binned by a factor of 2 for clarity. We attribute the narrow emission lines (marked with gray dotted lines) to the underlying star-forming region in the Cartwheel Galaxy. The strongest telluric feature is marked with the  $\oplus$  symbol. The remaining features can be explained by P Cygni profiles of hydrogen, helium, and Ca II. The broad, deep, asymmetric hydrogen absorption feature, the high helium-to-hydrogen line ratio, and relatively red continuum suggest a Type IIb classification for SN 2021afdx, although we never observe the hydrogen feature fully disappear. (The data used to create this figure are available.)

in Figure 3, where we compare to early spectra of the Type IIb SN 2016gkg (Tartaglia et al. 2017) and the

Type II SN 2021yja (Hosseinzadeh et al. 2022). The helium-to-hydrogen line ratio is also high and increasing in our spectral series, suggesting that the hydrogen features might have faded after the end of our observing campaign. Our earliest spectrum of SN 2021afdx is redder (Figure 3) and the photospheric temperature is lower (Figure 2, bottom) than typical SNe II at this phase. Lastly, the gradual rise and decline of the bolometric light curve of SN 2021afdx more closely resembles the Type IIb SN 1993J<sup>1</sup> than the Type II SN 2021yja (Hosseinzadeh et al. 2022), which rose quickly to a plateau (see Figure 2, center). However, as we never see the hydrogen features fully disappear, even by day 60, and our light curve does not extend to late enough times to observe a potential fall from plateau ( $\sim 100$  days), we cannot rule out a fast-declining SN II (i.e., a SN IIL) with some spectroscopic peculiarities. Our analysis does not depend strongly on the SN type, other than that it is the core collapse of a massive star, so we proceed by using the broader term (SN II) and comparing to both SNe II and IIb whenever possible.

We measure the photospheric velocity by fitting the sum of two equal-width Gaussians, one positive and one negative, and a linear continuum to the  $H\alpha$  feature in each of the first five spectra. The signal-to-noise ratio in the last spectrum is too low to confidently fit the absorption component. We use an MCMC routine with uniform priors on the centers of the Gaussians and the continuum intercept and log-uniform priors on the amplitudes and width of the Gaussians and the continuum slope. We report the means and standard deviations of the velocity posteriors, as calculated from the maximum and minimum of the model minus the continuum, in Table 1. The mean and standard deviation of these five measurements is  $v_{ej} \approx 11.9 \pm 0.5$  Mm s<sup>-1</sup>. Figure 2 (bottom) shows that this velocity is consistent with the photospheric radii around peak.

## 2.2. Space-based Infrared

We downloaded the JWST images of the Cartwheel Galaxy in ten filters spanning 0.9–18  $\mu\text{m}$  from the Mikulski Archive for Space Telescopes (Proposal 2727; PI: Pontoppidan; DOI: 10.17909/2n49-hx69) and performed aperture photometry using Photutils (Bradley et al. 2022). For NIRCcam, we used a circular aperture containing 80% of the PSF energy. For MIRI, we used a circular aperture containing 50% of the PSF energy, to avoid contamination from the star-forming region. We

<sup>1</sup> We constructed the pseudobolometric light curve of SN 1993J using data from Okyudo et al. (1993), van Driel et al. (1993), Benson et al. (1994), Lewis et al. (1994), Richmond et al. (1994, 1996), Barbon et al. (1995), and Metlova et al. (1995).

**Table 2.** JWST Observations and Photometry

| MJD       | Instrument | Filter | Exp. (s) <sup>a</sup> | Magnitude          |
|-----------|------------|--------|-----------------------|--------------------|
| 59742.131 | NIRCcam    | F090W  | 2748.616              | 23.944 $\pm$ 0.021 |
| 59742.172 | NIRCcam    | F150W  | 2748.616              | 23.242 $\pm$ 0.007 |
| 59742.214 | NIRCcam    | F200W  | 2748.616              | 23.093 $\pm$ 0.005 |
| 59742.131 | NIRCcam    | F277W  | 2748.616              | 23.287 $\pm$ 0.004 |
| 59742.172 | NIRCcam    | F356W  | 2748.616              | 23.128 $\pm$ 0.008 |
| 59742.214 | NIRCcam    | F444W  | 2748.616              | 22.223 $\pm$ 0.005 |
| 59745.322 | MIRI       | F770W  | 4040.464              | 21.497 $\pm$ 0.016 |
| 59745.354 | MIRI       | F1000W | 4040.464              | 21.366 $\pm$ 0.011 |
| 59745.388 | MIRI       | F1280W | 4040.464              | 21.141 $\pm$ 0.029 |
| 59745.420 | MIRI       | F1800W | 4084.864              | 21.823 $\pm$ 0.097 |

<sup>a</sup>Effective exposure time, corrected for dead time and lost time.

then applied aperture corrections from the JWST Calibration Reference Data System (CRDS; Greenfield & Miller 2016). Table 2 lists the results, given in AB magnitudes, and Figure 4 shows cutouts of these ten images centered on the SN.

The galaxy background in this region is complicated, and in the longer-wavelength filters the flux in the aperture is dominated by instrumental background. Thus, careful background subtraction is required. We chose two  $3 \times 3$ -pixel squares directly above and below the aperture (roughly perpendicular to the nearby star-forming region) and estimated the background level and its uncertainty by taking the median and the median absolute deviation, respectively, of those 18 pixels. Figure 4 shows the source and background apertures in each image. We subtracted the background level from each pixel in the aperture and added the background uncertainty in quadrature to the error images provided. The choice of the background level may explain the discrepancy between our measurements and the preliminary photometry of Engesser et al. (2022).

At the time of our analysis, the MIRI aperture corrections had been updated using in-flight data (`jwst_miri_apcorr_0008.fits`), but the NIRCcam aperture corrections had not (`jwst_nircam_apcorr_0004.fits`). In addition, the zero-point calibrations of both instruments suffer from uncertainties relative to preflight expectations. Boyer et al. (2022) report time-variable offsets of 1–23% in the eight NIRCcam detectors, and the most recent reduced MIRI images suffer from imperfect flat fielding of up to  $\approx 5\%$  uncertainty in flux values. The data at  $>18$   $\mu\text{m}$  has an additional uncertainty on flux zero-point, as their lin-

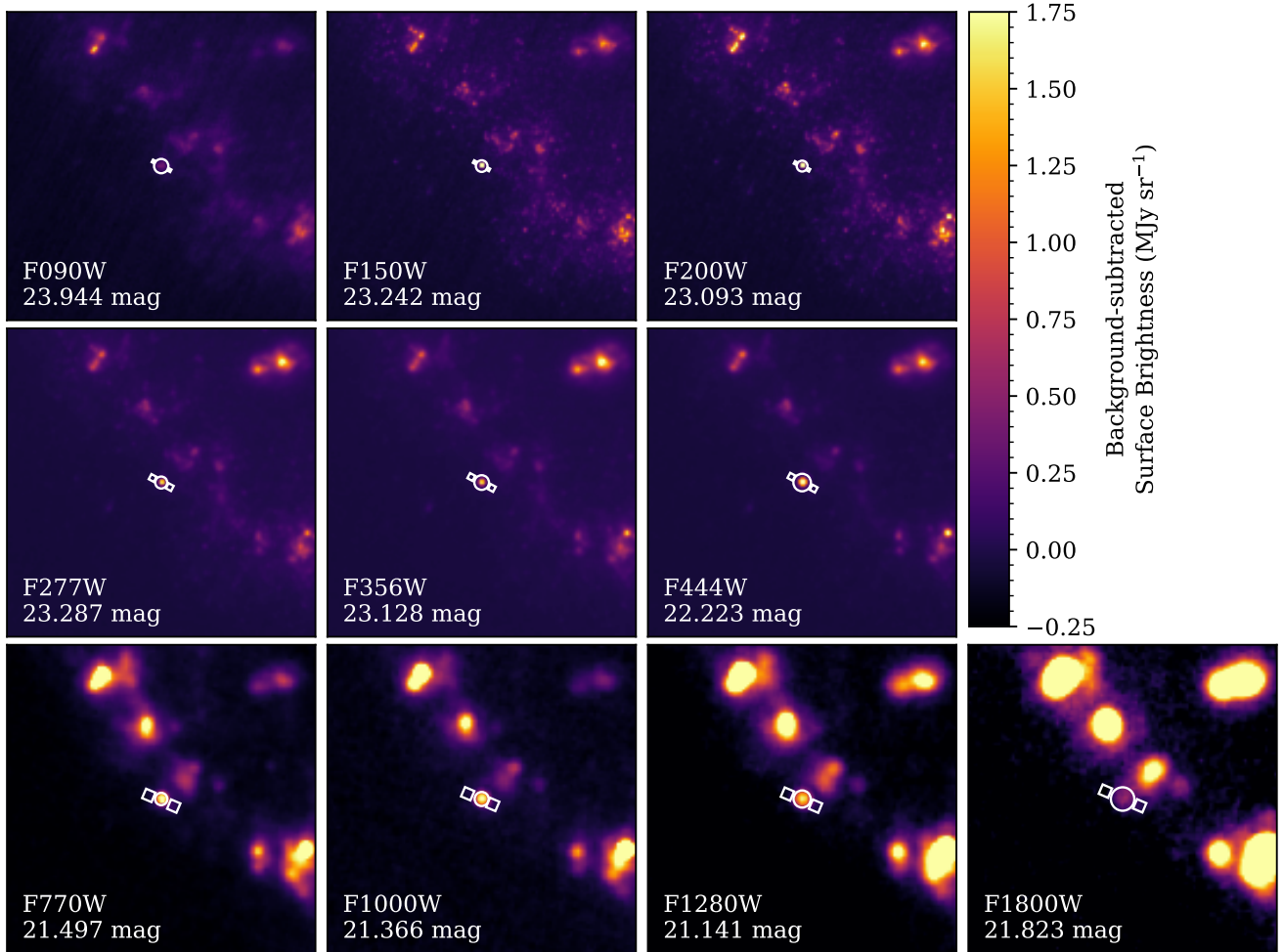


**Figure 4.**  $10'' \times 10''$  cutouts of JWST images of the Cartwheel Galaxy centered on SN 2021afdx in ten filters. The images are in their native resolution but have been resampled to have north up and east to the left. White circles mark the aperture used for photometry. White squares mark the region used for background subtraction. The filter name and SN brightness (in AB magnitudes) are reported in the lower left corner of each panel.

earity correction coefficients have not yet been updated based on inflight data. We choose to proceed with the official zero-points from CRDS (version 11.16.3), keeping in mind that our results can be re-evaluated in the future when more accurate calibrations are established.

### 3. DUST MODELING

Figure 5 shows the infrared SED of SN 2021afdx at a phase of 197–200 rest-frame days. The most notable feature is a peak in  $F_\lambda$  at  $4\text{--}7\ \mu\text{m}$ , a second emission component that may indicate dust associated with the SN.

We model the SED as a hot blackbody with temperature  $T_{\text{phot}}$  and radius  $R_{\text{phot}}$  plus a uniform sphere of warm dust with temperature  $T_{\text{dust}}$ , radius  $R_{\text{dust}}$ , and optical depth  $\tau_{18\ \mu\text{m}}$  at  $18\ \mu\text{m}$ . We chose this parametrization because the dust sphere will be optically thick at all

observed wavelengths if  $\tau_{18\ \mu\text{m}} > 1$ . The dust emission follows Osterbrock (1989, Appendix 2):

$$L_\nu = L_{\nu,\text{bb}} \left[ 1 - \frac{1}{2\tau_\nu^2} + \left( \frac{1}{\tau_\nu} + \frac{1}{2\tau_\nu^2} \right) e^{-2\tau_\nu} \right], \quad (1)$$

where  $L_{\nu,\text{bb}}$  is the spectral luminosity of a blackbody,

$$L_{\nu,\text{bb}} = 4\pi R_{\text{dust}}^2 \frac{2\pi h\nu^3}{c^2} \frac{1}{e^{\frac{h\nu}{k_B T_{\text{dust}}}} - 1}, \quad (2)$$

and  $\tau_\nu = \tau_{18\ \mu\text{m}} \frac{\kappa_\nu}{\kappa_{18\ \mu\text{m}}}$  is the frequency-dependent optical depth of the dust. We adopt the frequency-dependent opacity  $\kappa_\nu$  of  $0.1\ \mu\text{m}$  graphite dust from Fox et al. (2010), who give  $\kappa_{18\ \mu\text{m}} = 149\ \text{cm}^2\ \text{g}^{-1}$ . Our results are not sensitive to the choice of dust, except, crucially, for the total dust mass, which is inversely proportional to the dust opacity:

$$M_{\text{dust}} = \frac{4}{3}\pi R_{\text{dust}}^2 \frac{\tau_{18\ \mu\text{m}}}{\kappa_{18\ \mu\text{m}}}. \quad (3)$$

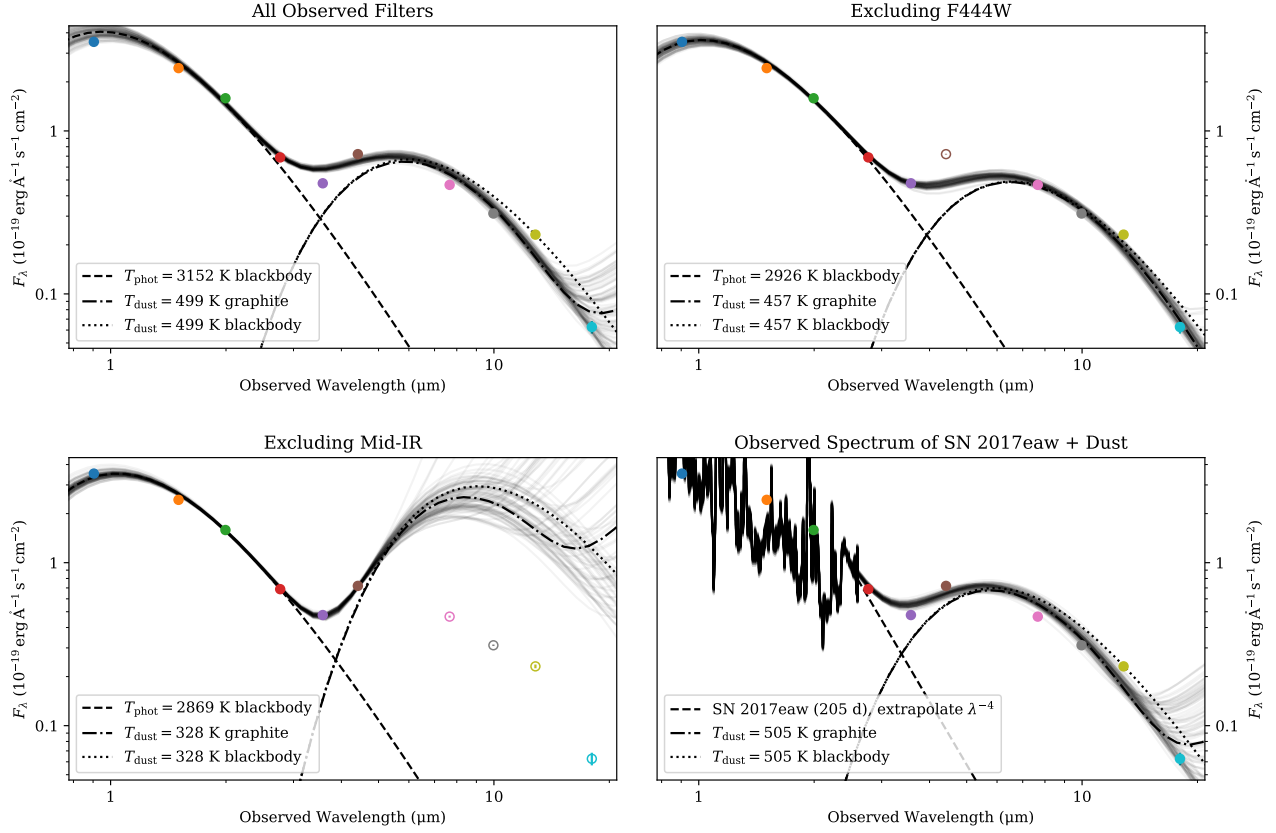


**Figure 5.** Top left: The infrared SED of SN 2021afdx at a phase of 197–200 rest-frame days (circles), compared to models of dust emission (solid lines). The dashed line shows the hot blackbody component and the dot-dashed line shows the warm graphite dust component. The dotted line shows a blackbody with the same temperature and radius as the dust. The blackbody plus dust model describes our observations well. Top right: Same as left, but excluding F444W from the fit (open circle). This filter may be contaminated by carbon monoxide emission. Excluding it gives a slightly better fit to the remaining data points, so we adopt this as our preferred model. Bottom left: Same as above, but excluding all filters redward of F444W (open circles), i.e., all the mid-infrared observations. This wavelength coverage is analogous to previous SN observations with the Spitzer Warm Mission. The dust SED is very poorly constrained and is not consistent with our mid-infrared observations, leading to incorrect inferences about the dust properties. Bottom right: Same as others, but using the observed spectrum of SN 2017eaw (Rho et al. 2018), extrapolated as  $\lambda^{-4}$  (dashed line), to model the near-IR filters. The resulting dust parameters are nearly identical to the blackbody fit (top left) but with a slightly higher intrinsic scatter.

**Table 3.** Dust Model Parameters

| Parameter                         | Prior                                | $1\sigma$ Equal-tailed Credible Interval |                        |                       |                       | Unit             |
|-----------------------------------|--------------------------------------|--|------------------------|-----------------------|-----------------------|------------------|
|                                   |                                      | All Filters                              | No F444W               | No Mid-IR             | SN 2017eaw            |                  |
| Photospheric temperature          | Uniform(0.1, 100)                    | $3.2 \pm 0.1$                            | $2.93^{+0.06}_{-0.05}$ | $2.87 \pm 0.04$       | ...                   | kK               |
| Photospheric radius               | Log-uniform(0.01, 1000)              | $6.1 \pm 0.3$                            | $6.9 \pm 0.2$          | $7.2 \pm 0.2$         | ...                   | $1000 R_{\odot}$ |
| Dust temperature                  | Uniform(0.1, 100)                    | $0.50 \pm 0.01$                          | $0.457 \pm 0.009$      | $0.33 \pm 0.01$       | $0.51 \pm 0.01$       | kK               |
| Dust radius                       | Log-uniform(0.01, 1000) <sup>a</sup> | $250 \pm 20$                             | $270 \pm 10$           | $1500^{+400}_{-300}$  | $250 \pm 20$          | $1000 R_{\odot}$ |
| Optical depth at $18 \mu\text{m}$ | Log-uniform(0.001, 2)                | $0.6^{+0.3}_{-0.1}$                      | $1.3 \pm 0.5$          | $0.5^{+0.7}_{-0.3}$   | $0.6^{+0.4}_{-0.1}$   | ...              |
| Intrinsic scatter                 | Half-Gaussian(max=10) <sup>a</sup>   | $6.6 \pm 0.5$                            | $3.7^{+0.5}_{-0.4}$    | $3.2^{+0.6}_{-0.5}$   | $8.9 \pm 0.5$         | ...              |
| Dust mass ( $3\sigma$ limits)     | Derived                              | $>1.6 \times 10^{-3}$                    | $>2.8 \times 10^{-3}$  | $>1.5 \times 10^{-2}$ | $>1.4 \times 10^{-3}$ | $M_{\odot}$      |

<sup>a</sup>For the fit excluding the mid-IR filters, we extend the maximum on  $R_{\text{dust}}$  to  $10^7 R_{\odot}$  and reduce the prior on  $\sigma$  to 6.

For example, if we had adopted amorphous carbon dust, with  $\kappa_{18\ \mu\text{m}} = 2140\ \text{cm}^2\ \text{g}^{-1}$  (Colangeli et al. 1995), all of our masses would be more than an order of magnitude lower.

We fit this model to the observed SED using an MCMC routine implemented in the Light Curve Fitting package (Hosseinzadeh & Gomez 2020). The model is very insensitive to  $\tau_{18\ \mu\text{m}}$  when  $\tau_{18\ \mu\text{m}} > 1$ , i.e., when the dust is optically thick, so we constrain  $\tau_{18\ \mu\text{m}} < 2$  using the prior. If the posterior probability density at  $\tau_{18\ \mu\text{m}} = 1$  is not negligible, we should consider  $\tau_{18\ \mu\text{m}} \gtrsim 1$  to be a lower limit. We also include an intrinsic scatter term,  $\sigma$ , that accounts for uncertainties in the model (e.g., line emission) by inflating the error bars on each data point by a factor of  $\sqrt{1 + \sigma^2}$ . We run 20 walkers for 1000 steps to reach convergence and then another 1000 steps to sample the posterior. Table 3 lists the model parameters, their priors, and their best-fit values (median and  $1\sigma$  equal-tailed credible interval). The best-fit model, as well as a breakdown of the two components, is shown in Figure 5 (top left).

SNe II (including SNe I Ib) are known to produce carbon monoxide (CO) during the nebular phase (e.g., Catchpole et al. 1988; Spyromilio et al. 1988; Spyromilio & Leibundgut 1996; Ergon et al. 2015), whose fundamental rovibrational transition emits around  $4.6\ \mu\text{m}$ . If CO is present in SN 2021afdx, this will produce an excess in our F444W observation with respect to the dust model. Therefore we repeat the above modeling procedure excluding this filter. Figure 5 (top right) and Table 3 show the results. This indeed achieves a better fit ( $\sigma = 3.6$  vs. 6.7) with a slightly lower dust temperature, undershooting F444W. We therefore adopt these results as our preferred set of parameters and claim a tentative detection of CO.

As a demonstration of the power of JWST in the mid-IR, we also repeat the fit excluding the four mid-IR filters (F770W, F1000W, F1280W, and F1800W). This fit simulates a data set from the Spitzer Warm Mission, the best infrared data available over the past decade. Figure 5 (bottom left) and Table 3 show that the dust SED is very poorly constrained without the mid-IR data points, and it leads to incorrect inferences about the dust properties.

At  $\approx 200$  days, the near-IR SEDs of SNe may not be well approximated by a blackbody, due to strong nebular emission lines. Therefore, as a final check, we repeat the fit using a model in which the hot blackbody is replaced by the observed spectrum of the Type II SN 2017eaw at 205 days after explosion from Rho et al. (2018), multiplied by a constant. We extrapolate from 2.52 to  $19.5\ \mu\text{m}$  (although it is negligible at  $\gtrsim 5\ \mu\text{m}$ )

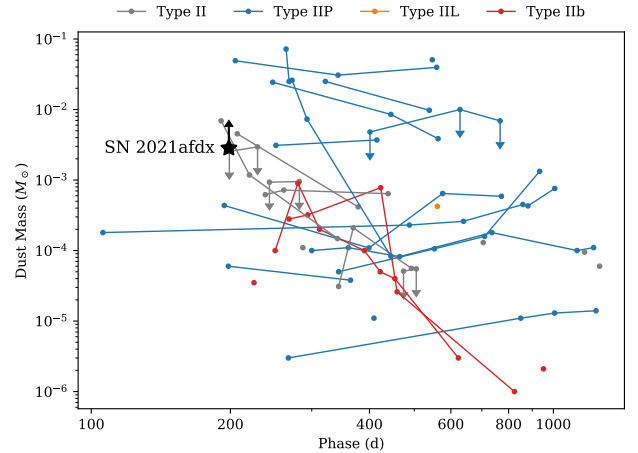


**Figure 6.** Dust masses in SNe II observed by Spitzer (circles) from Szalai et al. (2019). Lines connect multiple measurements for individual SNe, and downward-pointing arrows indicate upper limits on dust masses when reference images for subtraction were not available. The lower limit on the dust mass of SN 2021afdx measured here (black star) is consistent with most of their distribution. Notably, our limit is higher than the dust masses in any of the previously observed SNe I Ib, although the sample size is small.

using a  $\lambda^{-4}$  power law (Rayleigh 1900) matched to the red tail of the observed spectrum. The results, shown in Figure 5 (bottom right) and Table 3, give nearly identical dust parameters to the original fit with a blackbody, but with slightly higher intrinsic scatter.

Because the dust is optically thick, we can only place a lower limit on the total dust mass using Equation 3 (see, e.g., Meikle et al. 2007). The  $3\sigma$  limit (0.15th percentile of the posterior) on the dust mass is  $> 2.8 \times 10^{-3} M_{\odot}$ . This is consistent with most of the distribution of SN II dust masses from Szalai et al. (2019), although almost all of their observations are at later phases than ours (see Figure 6). Notably, our limit is higher than the dust masses in any of the four SNe I Ib observed by Szalai et al. (2019). The significance of this result will only become clear with larger sample sizes of the rarer subclasses of core-collapse SNe.

#### 4. DUST FORMATION SCENARIOS

Given these measurements, we investigate whether the dust that we observe is newly formed in the SN ejecta or whether it existed in the circumstellar environment prior to explosion. Optical observations at this phase could show the effect of dust extinction on the broadband light curve or the spectroscopic line profiles, but at this late phase, SN 2021afdx is beyond the reach of most ground-based telescopes. Therefore we must rely only on the parameters from our IR SED modeling. In

the newly formed dust scenario, we would expect the dust radius to be consistent with the ejecta radius and the dust temperature to be near the condensation temperature. However, if the grain size is large or the dust is clumpy or nonspherical, the radius from our model is only a lower limit.

Using the mean H $\alpha$  velocities from Section 2.1 and assuming homologous expansion, we estimate the ejecta position to be  $R_{\text{ej}}(t) = v_{\text{ej}}t = (2.9 \pm 0.1) \times 10^5 R_{\odot}$ , which is consistent with the dust radius from Section 3 if we assume a nonclumpy distribution of small-grained dust. Theory predicts the condensation temperature for carbonaceous dust to be  $\gtrsim 1600$  K (Gall et al. 2011b), about three times our measured dust temperature. However, astrophysical evidence from both massive stars (e.g., Beasor & Davies 2016; Lau et al. 2021) and supernovae (e.g., Tinyanont et al. 2016; Szalai et al. 2019) points to condensation temperatures below 1000 K. Therefore we consider our observations to be fully consistent with the newly formed dust scenario.

The alternative is that we are seeing an IR echo (e.g., Bode & Evans 1980; Dwek 1983; Graham & Meikle 1986; Meikle et al. 2006) off of pre-existing dust in the circumstellar environment. We can check the consistency of this scenario with an equilibrium calculation: each dust grain must emit as much energy as it absorbs. The luminosity emitted by an individual dust grain with radius  $a = 0.1 \mu\text{m}$  and temperature  $T_{\text{dust}} = 457$  K is

$$L_{\text{em}} = 4\pi a^2 \sigma_{\text{SB}} T_{\text{dust}}^4 Q_{\text{em}} = 9.6 \times 10^{-5} \text{ erg s}^{-1}, \quad (4)$$

where  $Q_{\text{em}}$  is the emission efficiency for graphite dust from Fox et al. (2010, their Figure 4) averaged over the emitted radiation field:

$$Q_{\text{em}} = \frac{\int B_{\nu}(\nu, T_{\text{dust}}) Q_{\text{em}}(\nu) d\nu}{\int B_{\nu}(\nu, T_{\text{dust}}) d\nu} = 0.023. \quad (5)$$

The luminosity absorbed by this dust grain from a source with luminosity  $L_{\text{peak}} = 1.66 \times 10^{42} \text{ erg s}^{-1}$  and temperature  $T_{\text{peak}} = 6900$  K at a distance  $R_{\text{dust}}$  is

$$L_{\text{abs}} = \frac{L_{\text{peak}}}{4\pi R_{\text{dust}}^2} \pi a^2 Q_{\text{abs}}, \quad (6)$$

where  $Q_{\text{abs}}$  is the absorption efficiency for graphite dust from Laor & Draine (1993) averaged over the incident radiation field:

$$Q_{\text{abs}} = \frac{\int B_{\nu}(\nu, T_{\text{peak}}) Q_{\text{abs}}(\nu) d\nu}{\int B_{\nu}(\nu, T_{\text{peak}}) d\nu} = 1.2. \quad (7)$$

Setting Equation 4 equal to Equation 6, we can solve for the radius of the dust shell.<sup>2</sup> We find that the dust

<sup>2</sup> Note that the result is not fully independent of  $a$  because the efficiency curves depend on the dust grain size.

must lie at  $R_{\text{dust}} = 1.0 \times 10^7 R_{\odot} = 280$  light-days from the center of the explosion. This is a factor of  $\approx 40$  larger than the dust radius inferred from our SED modelling, but that estimate is only a lower limit if the dust is clumpy, aspherical, or composed primarily of large grains. Given the uncertainties in our rough estimate here, we cannot rule out this scenario. Still, there is some fine tuning required to match the measured dust radius with the ejecta radius in the IR echo scenario, so we favor the former scenario of newly formed dust.

A time series of nebular infrared observations of SN 2021afdx could show time evolution in the dust SED, which could allow us to distinguish between the two formation channels, although the dust emission will shift out of the mid-IR as the ejecta cool even further. Nonetheless, as JWST continues to constrain the dust properties of a growing sample of core-collapse SNe—keeping in mind that in many cases it can only place a lower limit on the dust mass—we will begin to fill in the picture of whether these SNe can fully account for dust formation in the early universe.

## 5. SUMMARY AND CONCLUSIONS

We have presented near- and mid-IR observations of SN 2021afdx taken with JWST. The unprecedented combination of wavelength coverage (0.9–18  $\mu\text{m}$ ) and sensitivity allow us to distinguish two distinct components in the nebular IR SED, which we attribute to hot gas and warm dust in the SN ejecta. By fitting models of dust emission to the SED, we place a limit on the mass of dust to be  $M_{\text{dust}} > 2.8 \times 10^{-3} M_{\odot}$ , which is fairly typical among core-collapse SNe at this phase and higher than all previously observed SNe IIB dust masses. However, it is not enough to account for the dust observed in the early Universe, unless the true dust mass is 2–3 orders of magnitude above our lower limit. We find that the radius of the dust sphere is consistent with the ejecta position at this phase, suggesting that the dust could be newly formed in the ejecta. However, we cannot rule out the possibility of an IR echo off of pre-existing dust in the progenitor environment without further observations.

This Letter demonstrates the power of JWST to constrain models of SN dust formation, a capability that has been missing since the Spitzer Cold Mission. Furthermore, SN 2021afdx is almost twice as distant as the farthest SN II observed by Spitzer in the nebular phase (Szalai et al. 2019), meaning that many more nebular SNe, including those of rarer subtypes (e.g., SNe IIB), will be observable by JWST in the coming years. This increased sample size will quickly begin to probe the

extent to which interstellar dust formation in the early Universe can be explained by SNe.

### ACKNOWLEDGMENTS

We thank Matteo Correnti for his JWST post-pipeline data analysis notebook,<sup>3</sup> which provided a starting point for our analysis, Samaporn Tinyanont for maintaining publicly available, machine-readable graphite opacity tables,<sup>4</sup> and Jeonghee Rho for providing her spectrum of SN 2017eaw. We also thank Emma Beasor and Ryan Lau for helpful discussions about dust formation.

This work is based on observations made with the NASA/ESA/CSA James Webb Space Telescope. The data were obtained from the Mikulski Archive for Space Telescopes at the Space Telescope Science Institute, which is operated by the Association of Universities for Research in Astronomy, Inc., under NASA contract NAS 5-03127 for JWST. These observations are associated with program #2727. The Early Release Observations and associated materials were developed, executed, and compiled by the ERO production team: Hannah Braun, Claire Blome, Matthew Brown, Margaret Carruthers, Dan Coe, Joseph DePasquale, Nestor Espinoza, Macarena Garcia Marin, Karl Gordon, Alaina Henry, Leah Hustak, Andi James, Ann Jenkins, Anton Koekemoer, Stephanie LaMassa, David Law, Alexandra Lockwood, Amaya Moro-Martin, Susan Mullally, Alyssa Pagan, Dani Player, Klaus Pontoppidan, Charles Proffitt, Christine Pulliam, Leah Ramsay, Swara Ravindranath, Neill Reid, Massimo Robberto, Elena Sabbi, Leonardo Ubeda. The EROs were also made possible

by the foundational efforts and support from the JWST instruments, STScI planning and scheduling, and Data Management teams. The authors acknowledge the ERO production team for developing their observing program with a zero-exclusive-access period. This work makes use of data from the Las Cumbres Observatory telescope network.

Time domain research by G.H, D.J.S, and the University of Arizona team is supported by NSF grants AST-1821987, 1813466, 1908972, and 2108032, and by the Heising-Simons Foundation under grant #2020-1864. Research by S.V. is supported by NSF grant AST-2008108. T.S. is supported by the NKFIH/OTKA FK-134432 grant of the National Research, Development and Innovation (NRDI) Office of Hungary, the János Bolyai Research Scholarship of the Hungarian Academy of Sciences, and the New National Excellence Program (ÚNKP-21-5) of the Ministry for Innovation and Technology of Hungary from the source of NRDI Fund. The Las Cumbres Observatory group is supported by NSF grants AST-1911225 and 1911151.

*Facilities:* ADS, JWST (MIRI, NIRCam), LCOGT (FLOYDS, Sinistro), OSC, NED, TNS.

*Software:* Astropy (Astropy Collaboration 2022), emcee (Foreman-Mackey et al. 2013), FLOYDS pipeline (Valenti et al. 2014), `lcogtsnpipe` (Valenti et al. 2016), Light Curve Fitting (Hosseinzadeh & Gomez 2020), JWST CRDS (Greenfield & Miller 2016), Photutils (Bradley et al. 2022), PyZOGY (Guevel & Hosseinzadeh 2017).

### REFERENCES

- Amram, P., Mendes de Oliveira, C., Boulesteix, J., & Balkowski, C. 1998, *A&A*, **330**, 881
- Andrews, J. E., Sugerman, B. E. K., Clayton, G. C., et al. 2011, *ApJ*, **731**, 47
- Arendt, R. G., Dwek, E., Kober, G., Rho, J., & Hwang, U. 2014, *ApJ*, **786**, 55
- Astropy Collaboration, Price-Whelan, A. M., Lim, P. L., et al. 2022, *ApJ*, **935**, 167
- Bakx, T. J. L. C., Tamura, Y., Hashimoto, T., et al. 2020, *MNRAS*, **493**, 4294
- Barbon, R., Benetti, S., Cappellaro, E., et al. 1995, *A&AS*, **110**, 513
- Barlow, M. J., Krause, O., Swinyard, B. M., et al. 2010, *A&A*, **518**, L138
- Beasor, E. R., & Davies, B. 2016, *MNRAS*, **463**, 1269
- Benson, P. J., Herbst, W., Salzer, J. J., et al. 1994, *AJ*, **107**, 1453
- Bertoldi, F., Cox, P., Neri, R., et al. 2003, *A&A*, **409**, L47
- Bode, M. F., & Evans, A. 1980, *MNRAS*, **193**, 21P
- Boyer, M. L., Anderson, J., Gennaro, M., et al. 2022, *RNAAS*, **6**, 191
- Bradley, L., Sipőcz, B., Robitaille, T., et al. 2022, Astropy/Photutils: 1.5.0, Zenodo, doi:10.5281/zenodo.6825092
- Brown, T. M., Baliber, N., Bianco, F. B., et al. 2013, *PASP*, **125**, 1031
- Buzzoni, B., Delabre, B., Dekker, H., et al. 1984, *Msngr*, **38**, 9
- Catchpole, R. M., Whitelock, P. A., Feast, M. W., et al. 1988, *MNRAS*, **231**, 75P
- Colangeli, L., Mennella, V., Palumbo, P., Rotundi, A., & Bussoletti, E. 1995, *A&AS*, **113**, 561
- Dwek, E. 1983, *ApJ*, **274**, 175
- Dwek, E., Galliano, F., & Jones, A. P. 2007, *ApJ*, **662**, 927
- Dwek, E., Sarangi, A., & Arendt, R. G. 2019, *ApJ*, **871**, L33
- Engesser, M., Smith, K., Chen, T., et al. 2022, *TNSAN*, **155**, 1
- Ergon, M., Jerkstrand, A., Sollerman, J., et al. 2015, *Astronomy & Astrophysics*, **580**, A142
- Fitzpatrick, E. L. 1999, *PASP*, **111**, 63
- Foreman-Mackey, D., Hogg, D. W., Lang, D., & Goodman, J. 2013, *PASP*, **125**, 306
- Fox, O. D., Chevalier, R. A., Dwek, E., et al. 2010, *ApJ*, **725**, 1768
- Gal-Yam, A. 2016, in Handbook of Supernovae, ed. A. W. Alsabti & P. Murdin (Cham: Springer)

<sup>3</sup> <https://jwst-docs.stsci.edu/jwst-post-pipeline-data-analysis/data-analysis-example-jupyter-notebooks>

<sup>4</sup> [https://github.com/stinyanont/sed\\_et\\_al](https://github.com/stinyanont/sed_et_al)

- Gall, C., Andersen, A. C., & Hjorth, J. 2011a, *A&A*, **528**, [A13](#)
- Gall, C., Hjorth, J., & Andersen, A. C. 2011b, *A&ARv*, **19**, [43](#)
- Gomez, H. L., Krause, O., Barlow, M. J., et al. 2012, *ApJ*, **760**, [96](#)
- Graham, J. R., & Meikle, W. P. S. 1986, *MNRAS*, **221**, [789](#)
- Greenfield, P., & Miller, T. 2016, *A&C*, **16**, [41](#)
- Guevel, D., & Hosseinzadeh, G. 2017, PyZOGY, Zenodo, doi:[10.5281/zenodo.1043973](#)
- Hashimoto, T., Inoue, A. K., Mawatari, K., et al. 2019, *PASJ*, **71**, [71](#)
- Henden, A. A., Welch, D. L., Terrell, D., & Levine, S. E. 2009, *AAS*, **41**, [407.02](#)
- Hosseinzadeh, G. 2022, JWST Images of the Cartwheel Galaxy, STScI/MAST, doi:[10.17909/2n49-hx69](#)
- Hosseinzadeh, G., & Gomez, S. 2020, Light Curve Fitting, Zenodo, doi:[10.5281/zenodo.4312178](#)
- Hosseinzadeh, G., Kilpatrick, C. D., Dong, Y., et al. 2022, *ApJ*, **935**, [31](#)
- Indebetouw, R., Matsuura, M., Dwek, E., et al. 2014, *ApJ*, **782**, [L2](#)
- Kotak, R., Meikle, P., van Dyk, S. D., Höflich, P. A., & Mattila, S. 2005, *ApJ*, **628**, [L123](#)
- Kotak, R., Meikle, P., Pozzo, M., et al. 2006, *ApJ*, **651**, [L117](#)
- Kotak, R., Meikle, W. P. S., Farrah, D., et al. 2009, *ApJ*, **704**, [306](#)
- Laor, A., & Draine, B. T. 1993, *ApJ*, **402**, [441](#)
- Lau, R. M., Herter, T. L., Morris, M. R., Li, Z., & Adams, J. D. 2015, *Sci*, **348**, [413](#)
- Lau, R. M., Hankins, M. J., Kasliwal, M. M., et al. 2021, *ApJ*, **909**, [113](#)
- Lewis, J. R., Walton, N. A., Meikle, W. P. S., et al. 1994, *MNRAS*, **266**, [L27](#)
- Matsuura, M., Dwek, E., Meixner, M., et al. 2011, *Sci*, **333**, [1258](#)
- Meikle, W. P. S., Mattila, S., Gerardy, C. L., et al. 2006, *ApJ*, **649**, [332](#)
- Meikle, W. P. S., Mattila, S., Pastorello, A., et al. 2007, *ApJ*, **665**, [608](#)
- Meikle, W. P. S., Kotak, R., Farrah, D., et al. 2011, *ApJ*, **732**, [109](#)
- Metlova, N. V., Tsvetkov, D. Y., Shugarov, S. Y., Esipov, V. F., & Pavlyuk, N. N. 1995, *AstL*, **21**, [598](#)
- Okyudo, M., Kato, T., Ishida, T., Tokimasa, N., & Yamaoka, H. 1993, *PASJ*, **45**, [L63](#)
- Osterbrock, D. E. 1989, *Astrophysics of Gaseous Nebulae and Active Galactic Nuclei* (Sausalito, California: University Science Books)
- Planck Collaboration, Aghanim, N., Akrami, Y., et al. 2020, *A&A*, **641**, [A6](#)
- Pontoppidan, K. M., Barrientes, J., Blome, C., et al. 2022, *ApJL*, **936**, [L14](#)
- Priestley, F. D., Bevan, A., Barlow, M. J., & De Looze, I. 2020, *MNRAS*, **497**, [2227](#)
- Ragosta, F., Carini, R., Tartaglia, L., Benetti, S., & Yaron, O. 2021a, *TNSCR*, **4035**, [1](#)
- Ragosta, F., Carini, R., Tartaglia, L., et al. 2021b, *TNSAN*, **298**, [1](#)
- Rayleigh, L. 1900, *PMag*, **49**, [539](#)
- Rho, J., Geballe, T. R., Banerjee, D. P. K., et al. 2018, *ApJ*, **864**, [L20](#)
- Richmond, M. W., Treffers, R. R., Filippenko, A. V., & Paik, Y. 1996, *AJ*, **112**, [732](#)
- Richmond, M. W., Treffers, R. R., Filippenko, A. V., et al. 1994, *AJ*, **107**, [1022](#)
- Rieke, G. H., Wright, G. S., Böker, T., et al. 2015, *PASP*, **127**, [584](#)
- Rieke, M. J., Kelly, D. M., & Horner, S. D. 2005, *Proc. SPIE*, **5904**, [590401](#)
- Schlafly, E. F., & Finkbeiner, D. P. 2011, *ApJ*, **737**, [103](#)
- Smartt, S. J. 2009, *ARA&A*, **47**, [63](#)
- Smartt, S. J., Valenti, S., Fraser, M., et al. 2015, *A&A*, **579**, [A40](#)
- Spyromilio, J., & Leibundgut, B. 1996, *MNRAS*, **283**, [L89](#)
- Spyromilio, J., Meikle, W. P. S., Learner, R. C. M., & Allen, D. A. 1988, *Natur*, **334**, [327](#)
- Szalai, T., & Vinkó, J. 2013, *A&A*, **549**, [A79](#)
- Szalai, T., Vinkó, J., Balog, Z., et al. 2011, *A&A*, **527**, [A61](#)
- Szalai, T., Zsíros, S., Fox, O. D., Pejcha, O., & Müller, T. 2019, *ApJS*, **241**, [38](#)
- Tartaglia, L., Fraser, M., Sand, D. J., et al. 2017, *ApJL*, **836**, [L12](#)
- Temim, T., Dwek, E., Arendt, R. G., et al. 2017, *ApJ*, **836**, [129](#)
- Tinyanont, S., Kasliwal, M. M., Fox, O. D., et al. 2016, *ApJ*, **833**, [231](#)
- Tonry, J., Denneau, L., Weiland, H., et al. 2021, *TNSTR*, **4000**, [1](#)
- Tonry, J. L., Denneau, L., Heinze, A. N., et al. 2018, *PASP*, **130**, [064505](#)
- Valenti, S., Sand, D., Pastorello, A., et al. 2014, *MNRAS*, **438**, [L101](#)
- Valenti, S., Howell, D. A., Stritzinger, M. D., et al. 2016, *MNRAS*, **459**, [3939](#)
- van Driel, W., Yoshida, S., Nakada, Y., et al. 1993, *PASJ*, **45**, [L59](#)
- Van Dyk, S. D. 2016, in *Handbook of Supernovae*, ed. A. W. Alsabti & P. Murdin (Cham: Springer)
- Wesson, R., & Bevan, A. 2021, *ApJ*, **923**, [148](#)